



Assessment of Ocean Bottom Pressure Variations in CMIP6 HighResMIP Simulations

Le Liu¹, Michael Schindelegger¹, Lara Börger¹, Judith Foth¹, and Junyang Gou²

¹Institute of Geodesy and Geoinformation, University of Bonn, Bonn, Germany

²Institute of Geodesy and Photogrammetry, ETH Zurich, Zurich, Switzerland

Correspondence: Le Liu (le.liu@igg.uni-bonn.de)

Abstract. Ocean bottom pressure (p_b) variations from high-resolution climate model simulations under the CMIP6 (Coupled Model Intercomparison Project Phase 6) HighResMIP protocol are potentially useful for oceanographic and space-geodetic research, but the overall signal content and accuracy of these p_b estimates have hitherto not been assessed. Here we compute monthly p_b fields from five CMIP6 HighResMIP models at $1/4^\circ$ grid spacing over both historical and future time spans and compare these data, in terms of temporal variance, against observation-based p_b estimates from a $1/4^\circ$ downscaled GRACE (Gravity Recovery and Climate Experiment) product and 23 bottom pressure recorders, mostly in the Pacific. The model results are qualitatively and quantitatively similar to the GRACE-based p_b variances, featuring—aside from eddy imprints—elevated amplitudes on continental shelves and in major abyssal plains of the Southern Ocean. Modeled p_b variance in these regions is ~ 10 – 80% higher and thus overestimated compared to GRACE, whereas underestimation relative to GRACE and the bottom pressure recorders prevails in more quiescent deep-ocean regions. We also form variance ratios of detrended p_b signals over 2030–2049 under a high-emission scenario relative to 1980–1999 for three selected models and find statistically significant increases of future p_b variance by ~ 30 – 50% across the Arctic and in eddy-rich regions of the South Atlantic. The strengthening is consistent with projected changes in high-latitude surface winds and, in the case of the South Atlantic, intensified Agulhas leakage. The study thus points to possibly new pathways for relating observed p_b variability from (future) satellite gravimetry missions to anthropogenic climate change.

1 Introduction

Ocean bottom pressure (p_b) measures the weight of the total water column exerted on the seafloor, and thus its variations are inherently linked to mass fluxes and redistribution in the Earth system. For example, contemporary increases in ocean mass and thus static p_b result from loss of land ice and continued groundwater depletion (Ludwigsen et al., 2024). Dynamic p_b signals, on the other hand, are largely driven by atmospheric forcing (e.g., Ponte, 1999; Boening et al., 2011; Petrick et al., 2014; Fukumori et al., 2015), but may also arise internally within the ocean through non-linear processes (Zhao et al., 2021). To the extent the ocean is in geostrophic balance, horizontal p_b gradients can be used to infer barotropic transport variability of deep currents (e.g., Makowski et al., 2015) or characteristics of the meridional overturning circulation (Hughes et al., 2018). Physical oceanography aside, knowledge of p_b variability is also essential in geodesy, particularly for de-aliasing purposes in



satellite gravimetry processing (Shihora et al., 2022; Schindelegger et al., 2021). In addition, ocean mass redistributions excite Earth rotation changes (e.g., Harker et al., 2021) and cause crustal loading signals that may mask geophysically more relevant effects in station position time series (van Dam et al., 2012).

Works in the noted disciplines have been served well by p_b estimates on a global scale from time-resolved satellite gravimetry (i.e., the Gravity Recovery and Climate Experiment, GRACE) and numerical ocean models. Pertinent model diagnostics are typically drawn from data-constrained or free simulations of the real ocean (e.g., Piecuch et al., 2015; Hughes et al., 2018; Androsov et al., 2020; Shihora et al., 2022; Ponte et al., 2024). With a few exceptions (Ponte et al., 2002; Bingham and Haines, 2005; Landerer et al., 2007), coupled climate models have so far played no role in studies of p_b variability and its implications, mainly because they are arbitrary in time. However, such synthetic mass change records are potentially useful as background fields in future gravimetry mission simulations to assess the error characteristics and science return of specific satellite constellations (Daras et al., 2024). Moreover, climate models can be used to delineate likely changes in surface mass variability that may form target signals for future satellite gravity missions (cf. Jensen et al., 2020). Whether or not there are any significant changes in dynamic p_b to expect in a warming world is an interesting question in its own right.

We are thus motivated to take a first look at p_b estimates from the latest realization of the Coupled Model Intercomparison Project (CMIP), i.e., CMIP6. Specifically, our objectives are to (i) validate the p_b diagnostics from CMIP6 experiments by comparing them in, a statistical sense, to observations, (ii) identify source models that could possibly serve as input for end-to-end satellite simulations, and (iii) test for likely future changes in p_b variability under a high-emission scenario. Although the coarse-resolution (~ 100 -km grid spacing) branch of CMIP6 would suffice most of these purposes, we here analyze the output of eddy-permitting (~ 25 -km) ocean models under the CMIP6 HighResMIP (CMIP6-HR) protocol. Horizontal model resolution in this range is generally advantageous for representing topographically constrained dynamics (e.g., Harker et al., 2021). It also admits transient eddy features, which have their own unique imprint on p_b (Bingham and Hughes, 2008; Hughes et al., 2018; Zhao et al., 2021). Eddy activity, in turn, is projected to change profoundly in the 21st century (Beech et al., 2022) and therefore may strengthen or weaken p_b variability in certain locations. In total, and for practical reasons, we consider five out of the seven complete institutional contributions to the CMIP6-HR activity (cf. Haarsma et al., 2016; Roberts et al., 2020). The specific time periods examined by us are 1980–2014, representing recent historical climatic conditions, and 2030–2949 in the near future. Given the monthly sampling of the data and the fact that model drift (Sen Gupta et al., 2013) precludes the study of trends, we exclusively analyze p_b signals at intraseasonal to interannual periods.

2 Data and methods

2.1 Climate model data

CMIP6-HR is an effort dedicated to the investigation of the role of horizontal resolution in CMIP-type climate simulations (Haarsma et al., 2016), see, e.g., Docquier et al. (2019), Roberts et al. (2020) or Shi et al. (2021) for valorizations of these simulations with respect to the ocean. We use the model outputs from the coupled historical runs (labeled as ‘hist-1950’ in HighResMIP), complemented by coupled scenario simulations (‘highres-future’) in several cases. The hist-1950 simulations



Table 1. Selected specifications of the CMIP6-HR models used in this study^a

	ECMWF-IFS	HadGEM3- GC31	CNRM-CM6-1	CMCC-CM2	EC-Earth3P
Short name	ECMWF	HadGEM	CNRM	CMCC	Earth3P
Resolution label	HR	HM	HR	VHR4	HR
Atmospheric model ^b	IFS cycle 43r1	UM GA7.0	ARPEGE-Climat6.3	CAM4	IFS cycle 36r4
Atmosphere resolution in km	25	50	35	25	50
<i>Ocean/sea ice</i>					
Ocean model	NEMO3.4	NEMO3.6	NEMO3.6	NEMO3.6	NEMO3.6
Horizontal resolution in ° (km)	1/4° (25 km)	1/4° (25 km)	1/4° (25 km)	1/4° (25 km)	1/4° (25 km)
No. vertical levels	75	75	75	50	75
Variant label	r1i1p1f1	r1i1p1f1	r1i1p1f2	r1i1p1f1	r3i1p2f1
Reference	Roberts et al. (2018)	Roberts et al. (2019)	Voltaire et al. (2019)	Cherchi et al. (2019)	Haarsma et al. (2020)

^aThe analysis window is 1980–2014 (hist-1950 experiment) and, in addition, 2030–2049 for the HadGEM, CNRM, and Earth3P highres-future experiments under SSP5-8.5.

^bAbbreviations: IFS (Integrated Forecasting System of the ECMWF), UM GA7.0 (Global Atmosphere 7.0 configuration of the Met Office Unified Model), ARPEGE (Action de Recherche Petite Echelle Grande Echelle), CAM4 (Community Atmosphere Model Version 4).

cover the period 1950–2014 and provide the initial conditions to highres-future, nominally integrated to the year 2050. External forcing fields comprise time-varying solar, volcanic, anthropogenic aerosol, ozone depletion, and greenhouse gas effects (Haarsma et al., 2016). For the highres-future simulations, these forcings follow the Representative Concentration Pathway 8.5 (i.e., high-end emission) scenario with Shared Socioeconomic Pathway 5 (SSP5, O'Neill et al., 2016) conditions, abbreviated as SSP5-8.5.

The five CMIP6-HR models examined in our work are ECMWF-IFS-HR (European Centre for Medium-Range Weather Forecasts Integrated Forecasts System), HadGEM3-GC3.1 (Hadley Centre Global Environment Model 3 – Global Coupled vn 3.1), CNRM-CM6-1 (Centre National de Recherches Météorologiques Climate Model version 6), CMCC-CM2 (Euro-Mediterranean Centre on Climate Change Coupled Climate Model version 2), and EC-Earth3P; see Table 1 for an overview. Ad hoc short names, used throughout the paper, are ECMWF, HadGEM, CNRM, CMCC, and Earth3P, respectively. Given the scope of our study, we focus on the high-resolution (label HR, HM, or VHR4) configuration of each model, comprising a horizontal grid spacing of 1/4° (~25 km) for the ocean and 25 to 50 km for the atmosphere. The selected models differ with regard to the atmospheric component but not for the ocean (Table 1); the ocean component in all five cases is NEMO (Nucleus for European Modelling of the Ocean, either version 3.4 or 3.6, Madec, 2016), a hydrostatic, primitive equation general circulation model. Processes and properties of the ocean are therefore represented very similarly in all five climate models. Hence,



any spread in p_b variability reported below rather bears on parameter uncertainty, internal variability, or structural uncertainty
75 in the atmospheric component. Values for selected parameters of the ocean component (e.g., viscosity and diffusivity) can be
found in Docquier et al. (2019) and Roberts et al. (2020).

To deduce each model's bottom pressure, we retrieve monthly mean fields for potential temperature (standard name 'theta'),
salinity ('so'), and sea surface height above geoid ('zos'). For the hist-1950 experiments, we focus on the last 35 simulation
80 13 years. Comparisons of signal variance, as attempted in this study, could also be done for non-overlapping time periods if
one assumes stationarity of the p_b variability at a given location. We will return to this assumption in the summary section. The
time span considered for the highres-future simulations is 2030–2049. These choices were made in view of data availability
and manageable data volumes.

2.2 Calculation of ocean bottom pressure anomalies

85 A mathematical expression for p_b , obtained by integrating the hydrostatic balance over full depth along the vertical coordinate
 z (positive upward), is (e.g., Gill and Niller, 1973; Ponte, 1999)

$$p_b = \int_{-H}^0 \rho g dz + \int_0^{\eta} \rho_0 g dz = \int_{-H}^0 \rho g dz + \rho_0 g \eta \quad (1)$$

where $\rho = \rho(z)$ is the (in situ) density of seawater with surface value ρ_0 , η represents the sea level anomaly, H is the local
water depth, and g is the acceleration due to gravity. While atmospheric pressure contributes to p_b in nature, it is not part of
the exchange variables between atmospheric and oceanic components of CMIP6-HR and therefore neglected in Eq. (1). We
90 perform the vertical integration on the native model grid and specifically derive the value of ρ at a given location from the
modeled potential temperature and salinity, using the Gibbs SeaWater Oceanographic Toolbox (McDougall and Barker, 2011).
Exact evaluation of Eq. (1) from CMIP6-HR data would also require each model's internal representation of bottom topography,
e.g., in the form of a three-dimensional array of wet and dry cell fractions (or partial cell thicknesses; see Adcroft et al., 1997;
Bernard et al., 2006). Given that these fractions are not provided in the CMIP6 archive, we calculate approximate versions
95 of them based on given layer thicknesses and the ETOPO1 bathymetry dataset (Amante and Eakins, 2009), interpolated to
the horizontal model grid. Although the information on the provenance of model bathymetries in CMIP6-HR is sketchy, the
HadGEM ocean component description (Storkey et al., 2018) explicitly points to ETOPO1, and that is indeed a standard choice
for NEMO simulations on the ORCA025 grid (cf. Börger et al., 2023).

We reduce the full bottom pressure to dynamic anomalies (also denoted p_b) by subtracting the time-mean pressure and
100 trend values at each grid point, along with the monthly-varying spatial average of p_b . Global ocean mass changes, which may
have physical and non-physical causes in numerical ocean models (e.g., Sen Gupta et al., 2013), are therefore not part of the
analyzed p_b variability. To convey some sense of how this variability is distributed across frequencies while also keeping the
description of the results compact, we consider (i) full-time series of detrended dynamic p_b and (ii) non-seasonal anomalies
obtained by removing least-squares fits of the annual and semiannual oscillations from the full-time series. Variant (ii) thus



105 emphasizes intraseasonal and interannual p_b signals. The seasonal cycle, which has been the subject of several recent GRACE and ocean model studies (e.g., Cheng et al., 2021; Chen et al., 2023; Ponte et al., 2024), is only treated in passing. Note that p_b has standard SI units (Pa) in our calculations but is expressed as centimeters of equivalent water height (EWH) below, assuming the same reference density (1025 kg m^{-3}) as in the GRACE data.

2.3 Downscaled GRACE product

110 The primary dataset for validating the CMIP6-HR bottom pressures is a high-resolution satellite-based p_b product (Gou et al., 2025), obtained by downscaling available monthly p_b anomalies from GRACE/Follow On (Tapley et al., 2019) beyond their typical effective resolution of $\sim 3^\circ$. This product, called GRACE-DS hereinafter, offers gridded p_b information from April 2002 to December 2020 on a $1/4^\circ \times 1/4^\circ$ grid, commensurate with the resolution of the CMIP6-HR models. The downscaling was realized using a self-supervised deep-learning algorithm, guided by p_b diagnostics from two eddy-permitting ocean reanalyses
115 (Lellouche et al., 2013; Zuo et al., 2017). In particular, spatial detail on sub-GRACE grid scales was obtained by maximizing similarities between the downscaled product and the reanalysis output, while constraining the solution to the original GRACE values at larger scales (Gou et al., 2025). The data fusion algorithm was further enhanced by supervision signals based on input features, comprising, e.g., wind stress and bathymetry. From the three downscaled solutions provided by Gou et al. (2024), we use the one based on GRACE mascons from the Center for Space Research (Save et al., 2016).

120 The temporal RMS (root-mean-square) of the monthly GRACE-DS fields at each grid point is depicted in Fig. 1 and discussed in relation to the CMIP6-HR p_b signal content in Sect. 3.2. As with the models, the GRACE-DS time series represents dynamic, detrended p_b anomalies. Sources of inconsistency between the two datasets are, among other effects, the absence of barometric pressure-driven p_b variability in the models (cf. Piecuch et al., 2022, $\lesssim 0.5 \text{ cm}$ in places) and seismic gravity/deformation signals associated with major earthquakes in GRACE-DS (e.g., Zhang et al., 2020). The largest such spurious
125 contribution to p_b , apparent in Fig. 1 around the Malay Peninsula, stems from the 2004 Sumatra-Andaman and 2012 Indian Ocean earthquakes. We approximately delimit the affected region based on insight from literature (De Linage et al., 2009) and enhanced ($\geq 2 \text{ cm}$) open-ocean p_b values, and exclude it from all direct comparisons to the model fields below.

2.4 In situ observations

We also compare the CMIP6-HR p_b diagnostics with direct seafloor pressure measurements from the DART[®] (Deep-ocean
130 Assessment and Reporting of Tsunamis) program (Bernard and Meinig, 2011). DART is a US-led tsunami early warning system comprising more than 50 active deep-ocean bottom pressure recorders (BPRs) located mainly along the Circum-Pacific belt. The DART data are disseminated in meters of EWH with a nominal sampling of 15 min. From the full network, we extract 23 stations with nearly continuous observations over an 11-year time span from 2013 to 2023. The year 2013 is a reasonable start date, as it marks the completion of a major upgrade to the DART technology (Bernard and Meinig, 2011). Each of the 23
135 time series is a concatenation of recordings from successive deployments in slightly different locations, typically differing by $O(10 \text{ m})$ in the overlying pressure. We process each of these segments individually, removing (i) 3 days of observations at the start and end of the time series, (ii) a fitted second-order polynomial (to account for sensor drift, cf. Poropat et al., 2018), (iii)

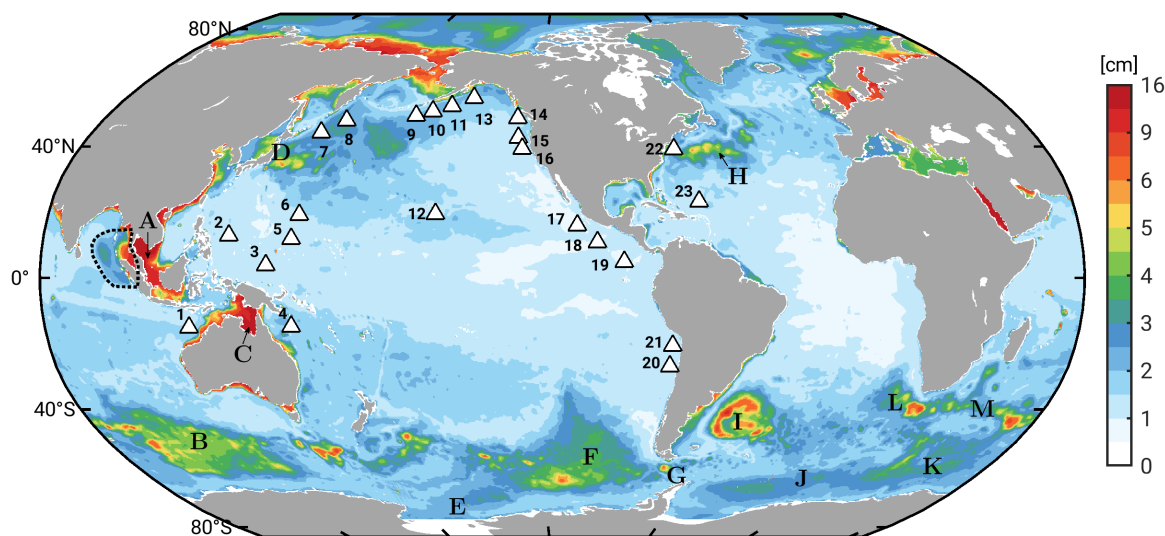


Figure 1. RMS of monthly p_b anomalies (in cm of EWH) from GRACE-DS, obtained by downscaling 1° GRACE mascons (Save et al., 2016) to a $1/4^\circ \times 1/4^\circ$ grid. Time series are from April 2002 to December 2020, with trends and spatial mean p_b signals removed. White triangles indicate the 23 BPR stations used in this study, labeled by increasing longitude. The dashed black polygon in the Andaman Sea marks the region excluded from the comparison in Sect. 3 due to the presence of seismic deformation signals in the GRACE fields. Lettered keys denote the (A) Gulf of Thailand, (B) Australian Antarctic Basin, (C) Gulf of Carpentaria, (D) Kuroshio Current, (E) Ross Sea, (F) Bellingshausen Basin, (G) Drake Passage, (H) Gulf Stream Extension, (I) Argentine Basin/Zapiola Gyre, (J) Weddell Basin, (K) Enderby Basin, (L) Cape Basin/Agulhas leakage, (M) Agulhas Return Current.

occasional spikes, and (iv) signals of 16 largest tidal constituents (Hart-Davis et al., 2021, including fortnightly, monthly, and semiannual constituents). Steps (i)–(iv) are applied to hourly-sampled versions of the segments, which we subsequently splice together and average into a monthly p_b series per station.

For consistency with our treatment of the CMIP6-HR fields (Sect. 2.1), the DART data should also be cleaned from global mean p_b signals, reflecting both atmospheric pressure variations over the ocean and true ocean mass changes (Ponte, 1993; Johnson and Chambers, 2013). While the former is readily corrected for using monthly sea level pressures from a modern atmospheric reanalysis (Hersbach et al., 2020), precise estimates for the mean ocean mass change over 2013–2023 are harder to come by. However, apart from a trend, these changes mainly consist of an annual oscillation, reaching ~ 0.5 cm in amplitude (Johnson and Chambers, 2013). We thus remove from the detrended DART data a synthetic time series of the seasonal cycle in ocean mass, constructed from p_b output (1992–2017) of an ocean state estimate (the Estimating the Circulation and Climate of the Ocean, Version 4 Release 4b, ECCOV4rb, Forget et al., 2015). ECCOV4rb is deemed suitable for this purpose, as it is constrained to most available oceanographic data, including GRACE-based p_b and observed global ocean mass changes.

Our final network, illustrated in Fig. 1, comprises 23 BPRs featuring a mean cumulative record length of 10.8 years, with monthly averages typically built from 260 to 350 days of valid observations per year. The in situ time is, therefore, much



shorter than the CMIP6-HR records but sufficiently long to constrain variability at the annual and higher frequencies (cf. Ray et al., 2021, for the case of sea level). Interannual p_b variability, which is less well represented by these ~ 10 -year records, accounts for about 30% of the variance in the full monthly DART time series. The network also heavily emphasizes the Pacific, with only two stations in the western North Atlantic and one sensor located in the Indian Ocean (North Australian Basin). We nevertheless prefer to perform our analysis based on a homogeneous, consistently processed in situ dataset and refrain from adding other BPR time series, which are usually short in duration ($\lesssim 1\text{--}4$ years, Poropat et al., 2018; Androsov et al., 2020; Schindelegger et al., 2021) or confined to special locations (e.g., the Arctic Beaufort Gyre, Kemp et al., 2005).

3 Results

3.1 Overview of modeled p_b variability

Figure 2 (left column) illustrates the RMS of monthly dynamic p_b anomalies, calculated for each of the five CMIP6-HR models over the period 1980–2014. The model results are qualitatively and quantitatively very similar to the p_b variability in the GRACE-DS product (Fig. 1), ocean state reconstructions (Piecuch et al., 2015; Gou et al., 2025), and ocean forward models forced by atmospheric analysis fields (e.g., Hughes et al., 2018; Poropat et al., 2018; Androsov et al., 2020). Among the defining features are a general increase in p_b variability from temperate to polar latitudes, elevated amplitudes in several marginal seas (e.g., Hudson Bay, Mediterranean Sea, Red Sea), and largest signals near continental boundaries. Shallow depths facilitate a vigorous barotropic response to the imposed wind stress (Vinogradova et al., 2007), leading to peak values of 10–15 cm in Fig. 2 over, e.g., the Siberian Shelf, Chukchi Sea, Gulf of Thailand, Gulf of Carpentaria, and Baltic Sea. In some of these places, coastally trapped waves contribute to the spreading of locally generated mass anomalies (e.g., Oliver and Thompson, 2011; Fukumori et al., 2015).

In the deep ocean, known regions of relatively high barotropic variability are the Arctic Ocean, the subpolar Northwest Pacific (Petrick et al., 2014), and the three major abyssal plains in the Southern Ocean (Bellingshausen, Australian-Antarctic, and Weddell-Enderby basins). These plains are encased by nearly closed contours of potential vorticity, thus trapping and amplifying forced barotropic circulations (e.g., Fukumori et al., 1998; Weijer and Gille, 2005; Ponte and Piecuch, 2014; Weijer, 2015). The Australian-Antarctic basin is the most energetic of the three regions, with RMS values of $\sim 4\text{--}6$ cm in all five models. Bottom topography also plays a key role in generating the characteristic, near-uniform fluctuation in p_b (up to 4 cm, Fig. 2) in the interconnected deep basins of the Arctic Ocean and Nordic Seas. In detail, wind stress along the continental slope results in cross-slope Ekman transport, which creates p_b anomalies of opposite sign between the shallow shelf and the adjacent deep ocean (Fukumori et al., 2015). The deep-ocean mass anomaly propagates away from its source regions as trapped Kelvin wave, separates from its shallow counterpart at straits and sills, and eventually equilibrates across the deep Arctic basins that are bounded by gradients of potential vorticity.

Forced barotropic dynamics aside, the CMIP6-HR models also contain an active mesoscale field, which can modulate the p_b diagnostics on local to basin-wide scales at intraseasonal and longer periods (Hughes et al., 2018; Zhao et al., 2021, 2023). Localized imprints of eddies and baroclinic instabilities are most obvious in western boundary current regions (Agulhas Retrore-

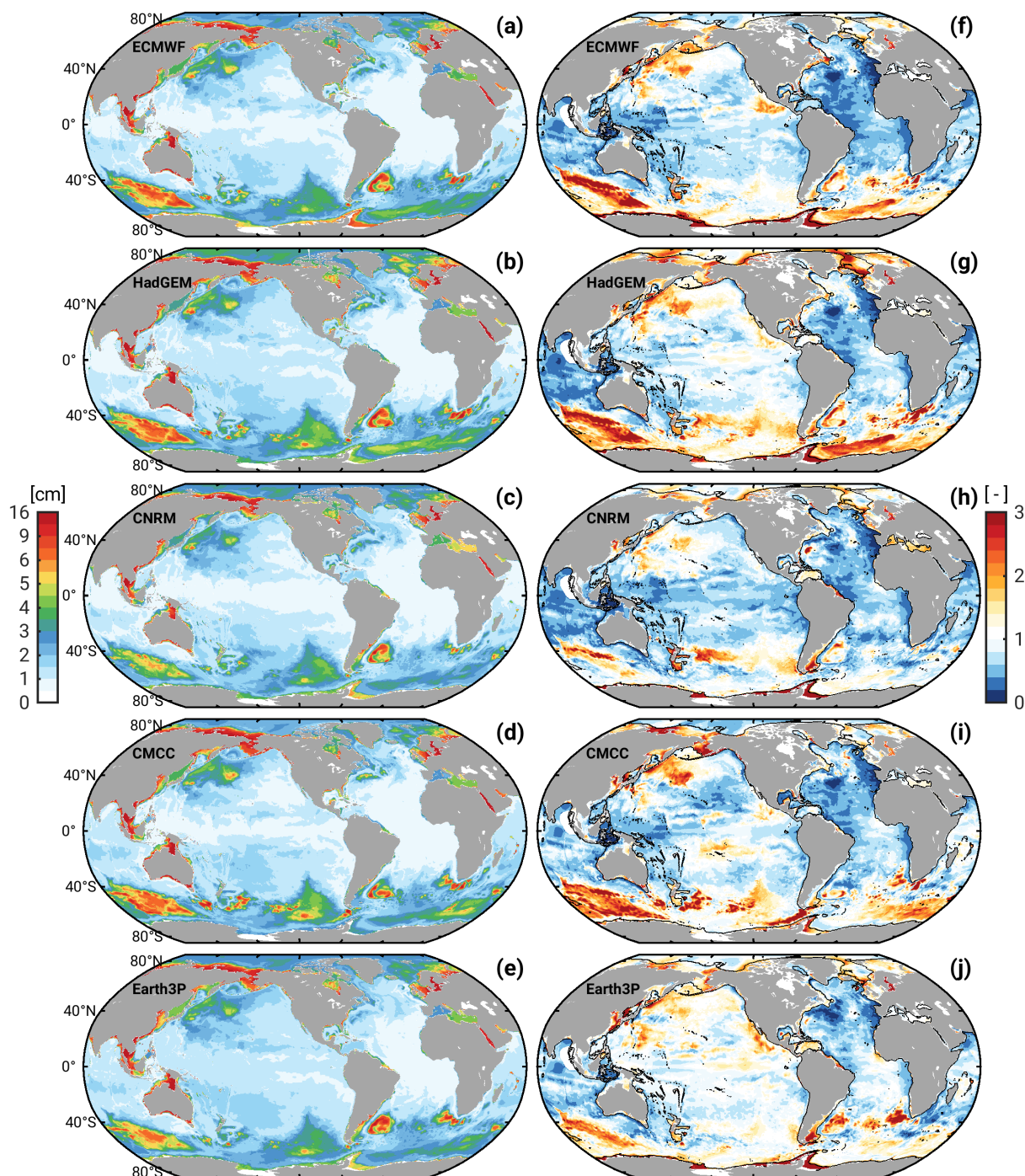


Figure 2. RMS (cm) of detrended p_b time series, 1980–2014, from five CMIP-HR models (left column) and each model’s variance ratio, R , relative to the p_b variance from GRACE-DS (right column). Values of $R > 1$ indicates an overestimation of bottom pressure variability in the model, while $R < 1$ suggests underestimation. The black solid line marks the 1000-m isobath, and the region of the Andaman Sea anomaly seen in GRACE-DS is masked out; cf. Fig. 1.



185 flexion, Kuroshio, Gulf Stream) and broadly along the path of the Antarctic Circumpolar Current (Androsov et al., 2020).
A stand-out feature in all models, perhaps with the exception of CMCC (Fig. 2d), is a ~8-cm G-shaped p_b structure in the
Argentine Basin. The pattern is the signature of the Zapiola Anticyclone, a well-known recirculation supported by high eddy
activity in the western parts of the basin and interactions of that eddy field with bottom topography (de Miranda et al., 1999;
Hughes et al., 2007). The GRACE-DS product suggests a similarly G-shaped structure around the Zapiola Drift (Fig. 1), albeit
190 largely inherited from the utilized ocean reanalyses rather than the GRACE gravity fields themselves (Gou et al., 2025).

3.2 Comparison with GRACE-DS – broadband variability

For a more quantitative analysis of the agreement between modeled and observation-based p_b fluctuations, we compute variance
ratios, R , defined as

$$R = \frac{\sigma_{mod}^2}{\sigma_{obs}^2} \quad (2)$$

where σ_{mod}^2 represents the p_b variance of a chosen model and σ_{obs}^2 is the observed variance at a given location, calculated
195 from GRACE-DS, or from BPRs below. Figure 2 (right column) illustrates global estimates of R for the full (i.e., unfiltered)
 p_b model time series relative to GRACE-DS, deduced after interpolating σ_{mod}^2 from the native model grid to the GRACE-DS
grid. Despite differences in detail, the five maps have several features in common. In particular, they suggest a tendency for
excess model variance ($R > 1$) in areas of enhanced p_b amplitudes (Fig. 2, left column), while underestimation by the models
($R < 1$) prevails in less energetic regions. One may argue that the latter is simply due to noise in the chosen GRACE product,
200 dominating the low and mid-latitude RMS in Fig. 1. However, random errors in a single monthly gravity field solution are
typically estimated to be 3–4 cm (e.g., Kvas et al., 2019), which limits the noise component on the temporal RMS in Fig. 1 to
0.3 cm (inferred from a pessimistic variance propagation over 192 monthly p_b fields).

Less easy to rebut is the existence of systematic effects in the GRACE-DS product, comprising, e.g., imperfect corrections
for low-degree zonal spherical harmonics and geocenter motion. In addition, GRACE-derived p_b estimates contain the effects
205 of gravitational attraction and loading (GAL). The physics of GAL are not encoded in CMIP6-HR but can induce ocean mass
changes in the order of 0.5 cm, particularly at the annual frequency and near continental boundaries (Ponte et al., 2024). Parts
of the higher variance in GRACE-DS in the Northern Indian Ocean and off the Amazon Shelf, which adjoin regions of large
terrestrial water storage variations, are therefore likely due to GAL. We also note that the underestimation of variance in the
deep-water tropics and some eastern boundary regions in CMIP6-HR (Fig. 2f–j) coincides with areas where p_b variability is
210 influenced by baroclinic dynamics and coupling between baroclinic and barotropic modes; cf. Hughes et al. (2018) but see also
Piecuch et al. (2015) and Zhao et al. (2021). Proper depiction of these processes in the models may pose a challenge, especially
in non-eddy-resolving configurations. Overall, we conclude that the dominance of $R < 1$ in quiescent ocean regions in Fig. 2
is due to a mixture of data noise, remaining systematic effects in the GRACE-DS fields, and mismodeled or entirely absent
 p_b signals in the simulations. Out of the five cases considered, HadGEM and Earth3P appear to be least affected by modeling
215 issues; global median variance ratios, \bar{R} , deduced from all grid points with a model RMS of ≤ 3 cm and in depths greater than



Table 2. Global median variance ratios, \bar{R} , of the CMIP6-HR models relative to GRACE-DS and BPRs^a

Model Name	GRACE-DS, deep		GRACE-DS, shelf		BPRs ^b
	RMS > 3 cm	RMS ≤ 3 cm	$ \phi > 60^\circ$	$ \phi \leq 60^\circ$	
ECMWF	1.54 (1.40)	0.72 (0.66)	1.39 (1.50)	1.11 (1.36)	1.05 (0.63)
HadGEM	1.52 (1.49)	0.82 (0.74)	1.86 (1.71)	1.30 (1.64)	1.04 (0.69)
CNRM	1.16 (1.11)	0.73 (0.62)	1.50 (1.53)	0.94 (1.20)	0.84 (0.60)
CMCC	1.78 (1.57)	0.74 (0.59)	1.38 (1.36)	1.19 (1.32)	0.76 (0.53)
Earth3P	1.32 (1.24)	0.91 (0.74)	1.49 (1.53)	1.25 (1.59)	1.26 (0.72)

^a For each model, we list the global median value of R , relative to GRACE-DS, in four regions, two regions each in deep water (depths > 1000 m) and shallow water (depths < 1000 m). The partitioning in the deep ocean is by model RMS (> 3 cm or ≤ 3 cm), while shelf regions are separated by latitude ϕ (higher or lower than 60°). Values in brackets are the same estimates for the non-seasonal signal content. The last column shows the median variance ratios relative to BPRs.

^b When compared to BPRs, GRACE-DS has a median variance ratio of 1.30 for the full time-series, and 0.92 for non-seasonal p_b changes.

1000 m, are 0.82 (HadGEM) and 0.91 (Earth3P). These numbers are considerably closer to 1 than for the other three models ($\bar{R} \approx 0.73$, Table 2).

Shifting the focus to the red (i.e., $R > 1$) patches in Fig. 2, we find that all models overestimate the p_b variance relative to GRACE-DS in the Northwest Pacific, the Australian-Antarctic Basin, and (to some extent) the Weddell-Enderby abyssal plain. Excess values are least pronounced in CNRM and largest in CMCC, evident also from the global median variance ratios taken over deep energetic regions ($\bar{R} = 1.16$ vs. $\bar{R} = 1.78$, see Table 2). Given the importance of wind stress curl and bottom topography in shaping the p_b variability in these deep basins (cf. Sect. 3.1), misrepresentation of either of these factors could reduce the fidelity of the modeled barotropic dynamics. For example, both the horizontal and vertical model resolution may be too coarse to produce the necessary topographic steering and dissipation by form stress (Weijer and Gille, 2005). Other suspects are imperfect wind stress parametrizations or overly strong surface winds as simulated by each model's atmosphere. However, supplementary checks of the 10-m wind speeds from several of the tested models revealed only small deviations from atmospheric reanalysis fields.

A propensity for excess p_b variance in the CMIP6-HR models is also seen for most continental shelf regions—in sub-polar and polar latitudes more so than in the tropics (cf., e.g., the Gulf of Thailand and Indonesian Seas). This geographical dependence is further brought out in Table 2, where we compute global median variance ratios in shallow water ($H < 1000$ m) both for latitudes higher and lower than 60° (a somewhat arbitrarily chosen cut-off). The overestimation of shallow p_b variations within 60° from the equator is rather subtle, bounded by $\bar{R} = 1.30$ for HadGEM. The HadGEM value increases to $\bar{R} = 1.86$ in polar latitudes, followed by $\bar{R} = 1.38$ – 1.50 in the other models. Common regions of systematic overestimation are the East Siberian Shelf, the Bering Sea, and the Antarctic continental shelf. While the red patches in the Arctic may again point to issues regarding wind stress forcing and dissipation mechanisms, the overestimated p_b variability in the Weddell and Ross Seas bears

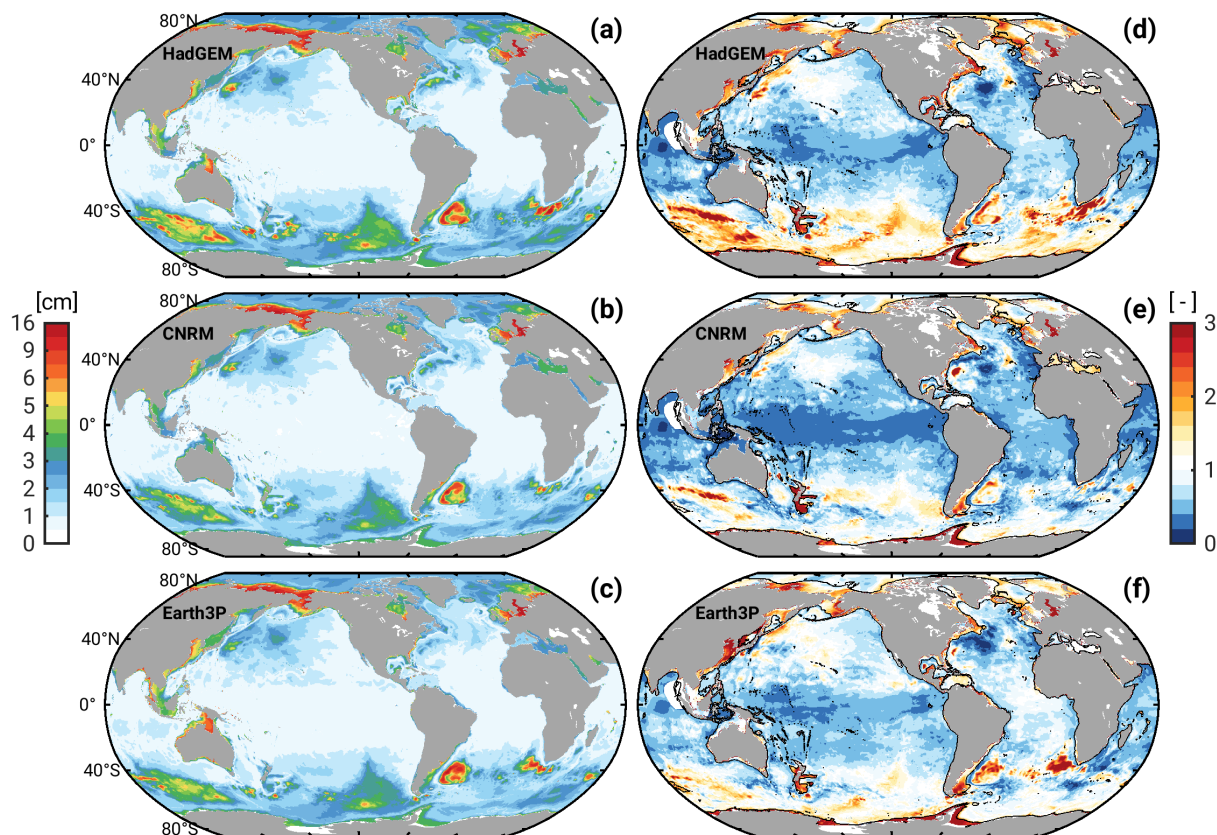


Figure 3. As in Fig. 2 but restricted to three models (HadGEM, CNRM, Earth3P) and non-seasonal signals.

on the blocking of Antarctic ice shelf cavities in CMIP6-HR. This modeling choice constricts the solution to a narrower body of water than in the real ocean and necessarily distorts the dynamics of the region.

As for the p_b imprints of mesoscale eddies, areas of over- and underestimation mostly vary from model to model, see, e.g., the Drake Passage or the Agulhas Retroreflection and its leakage to the west. However, at these small scales, the signal content in the GRACE-DS product is the result of trading off reanalyses output with GRACE fields that have an effective resolution of ~ 300 km (Gou et al., 2025). This type of blend certainly limits the validity of the comparison in Fig. 2 at the mesoscale. We nevertheless find a common patch of low variances ratios ($R \approx 0.5$) in the Northwest Atlantic south of Grand Banks, where the p_b signature of eddies in the GRACE-DS product spread considerably further into the Atlantic interior (Fig. 1) than in the CMIP6-HR models. The situation bears close resemblance to Figure 8 in Bernard et al. (2006), which suggests that NEMO simulations on the ORCA025 grid typically underestimate the magnitude and spatial spread of eddy kinetic energy in the Gulf Stream Extension.



3.3 Non-seasonal p_b variability

Modeled p_b variability with annual and semiannual oscillations subtracted is briefly assessed for three of the five available models. We select CNRM and Earth3P, which compare favorably to GRACE for energetic deep-ocean regions in Fig. 2, and HadGEM—essentially to have somewhat of a counterpoint to the other two models. Global median variance ratios at non-seasonal periods for all five models are compiled in Table 2. As evident from Fig. 3, removal of the seasonal cycle reduces RMS values in deep waters of temperate latitudes to ~ 1 cm. At these magnitudes, comparisons with GRACE-DS are likely limited by data noise and subtle systematic errors (cf. Sect. 3.2), inhibiting more solid inferences as to why variance ratios in quiet deep-ocean regions decrease relative to the full time series (Table 2, Fig. 2f–j vs. Fig. 3d–f). Non-seasonal signal levels in many of the more energetic areas in Fig. 3 remain comparable to the full variability (Fig. 2), and so do the variance ratios over GRACE-DS. Obvious examples are the Arctic Ocean and Nordic Seas, the Bellingshausen Basin, and several eddy-active regions (e.g., Zapiola Drift, Agulhas leakage, Gulf Stream Extension).

Wherever p_b has an appreciable seasonal cycle (cf. Ponte et al., 2024), RMS values in Fig. 3 are lower than in Fig. 2. Aside from numerous shelf areas, such as the Gulf of Thailand, non-seasonal amplitudes are also weaker than seasonal amplitudes in the Northwest Pacific, the Australian-Antarctic Basin, and the Weddell-Enderby Abyssal Plain. These changes go along with an improvement of the variance ratios relative to GRACE-DS toward $R \approx 1$ (even for HadGEM), suggesting that wind-driven geostrophic modes in abyssal-plain regions are indeed too energetic at seasonal periods in CMIP6-HR. Another noteworthy change as we switch from full to non-seasonal variability is the increase in global median variance ratios over mid- and low-latitude continental shelves by about 0.2 for each of the five models (Table 2). The increase is mainly caused by an excess of p_b variability relative to GRACE-DS in the shallow waters along the China and North American east coasts, as well as around New Zealand. For eastern continental boundaries, this overestimation potentially points to modeling problems regarding the propagation and decay of coastally trapped waves (Hughes et al., 2019).

3.4 Comparison with in situ observations

Comparisons against BPRs in terms of signal levels (RMS), variance ratios, and median variance ratios over all 23 sites are illustrated in Fig. 4 and Table 2. The analysis complements the previous validation against GRACE-DS in relatively quiet (RMS ≤ 3 cm) deep-ocean regions, emphasizing in particular the Pacific; cf. the BPR locations in Fig. 1. For additional context, we also include (but do not extensively discuss) point-wise statistics from GRACE-DS in Fig. 4. A first general observation is that the BPRs have signal levels very similar to those present in the model-based and GRACE-DS p_b estimates at the tested locations. Exceptions from this behavior are rather nuanced and also depend on whether unfiltered or non-seasonal signals (Fig. 4a–b) are analyzed. Specifically, we can discern a tendency for higher in situ than model p_b variance for several sites near the equator (IDs 1–5 and 19), i.e., latitudes where baroclinic and partly non-linear dynamics govern bottom pressure changes (Piecuch, 2015; Hughes et al., 2018). The phenomenon appears to be common to both the full and filtered time series at most of the noted stations.

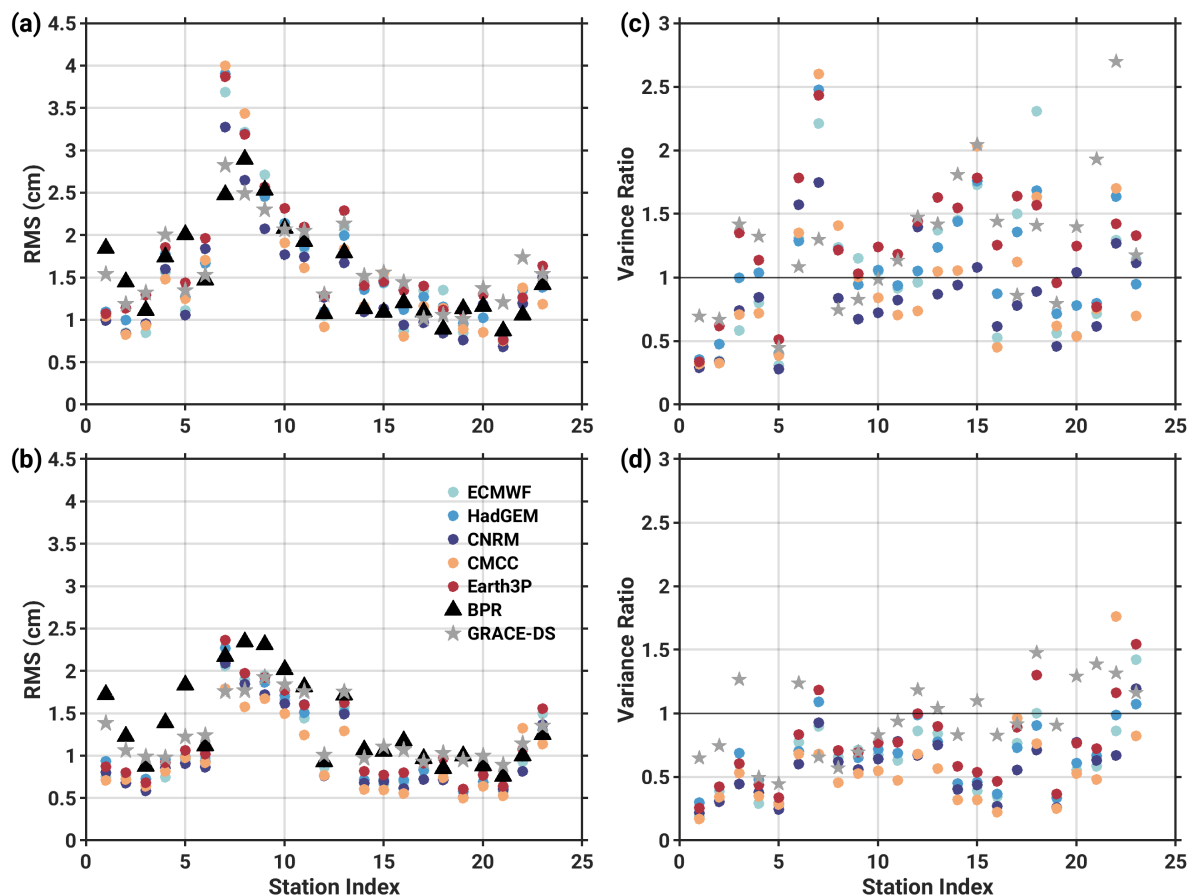


Figure 4. Comparison of the CMIP6-HR and GRACE-DS p_b variability against BPR observations at 23 locations (see Fig. 1) in terms of RMS (left panels) and variance ratios (right panels, $R = 1$ indicated by horizontal gray line). The top row shows the statistics for the full broadband p_b variations, while the bottom row is for non-seasonal signals.

Somewhat more puzzling, at least at first glance, is that for all sites in the North and Northeast Pacific (IDs 7–16, and partly
 280 elsewhere), the model variance ratios hover around 1–1.5 with the seasonal cycle included (Fig. 4c) but drop well below $R = 1$
 once it is eliminated (Fig. 4d). This contrast points to systematic differences between BPRs and models in their representation
 of seasonal p_b signals. At the points analyzed here, seasonal oscillations evidently make up a larger fraction of the overall p_b
 variance in the models than they do in the DART data. We suspect that at a resolution of $1/4^\circ$, the model bathymetry is too
 coarse (or too smooth) to capture the damping effects of small-scale topography on the p_b response to seasonal wind stress
 285 forcing; cf. Chen et al. (2023) for an in-depth study of the problem in the North Pacific Ocean. Accordingly, the apparent
 agreement between CMIP6-HR and the BPRs in the broadband case (Fig. 4a) may be partly coincidental; that is, anomalous
 seasonal variability in the models matches the variance due to non-seasonal local p_b fluctuations in the in situ series. On the
 subject of topography, a final interesting case is station 22 (DART ID 44402, Southeast Block Canyon), which sits at the lower



New England continental slope at a depth of about 2600 m. This setting likely suppresses mesoscale signals in bottom pressure
290 from the nearby Gulf Stream (Hughes et al., 2018), hence the diminished RMS in Fig. 4a. However, there is little hope that
such effects are represented accurately with ocean models run at ~ 25 -km grid spacings.

Adopting a more quantitative view, median variance ratios \bar{R} over all BPRs range from 0.76 (CMCC) to 1.25 (Earth3P) and
decrease to $\bar{R} = 0.53$ – 0.73 after removal of the seasonal cycle (Table 2). The comparison of CMIP6-HR with GRACE-DS on
a global scale suggests, in fact, very similar ranges and model rankings. This is a reassuring result that alleviates some of our
295 concerns as to the quality of the satellite-based p_b solutions at low signal levels (Sect. 3.3). Consistency in detail is particularly
seen along the North and East Pacific margins (IDs 9–20), where both GRACE-DS and the BPRs attribute lowest variance
ratios to either CNRM and CMCC and highest variance ratios to Earth3P (Figs. 2–4). Thus, the DART series offer a useful
point of comparison, despite their limited spatial coverage and the possible presence of short-scale signals in the records. Joint
consideration of the lumped statistics in Table 2 and the GRACE-DS variance ratio maps (Figs. 2–3) nevertheless suggest that
300 Earth3P outperforms the other models in most dynamical regimes. CNRM is least affected by the common issue of excess
 p_b variance in deep energetic regions, whereas HadGEM comes close to Earth3P in quiescent areas. We proceed with these
three models for the remainder of the analysis and note that while other choices would have been possible, the overall p_b
characteristics in all five models are still very similar.

3.5 Projected changes in p_b variability

305 We now examine whether the CMIP6-HR models suggest any notable changes in p_b variability under anthropogenic climate
change (Fig. 5). To that end, we compute variance ratios, R , of the detrended p_b series from the three previously selected models
over the time span 2030–2049 (highres-future) with respect to 1980–1999 (hist-1950 simulations). The mid-points of the two
windows are therefore 50 years apart, representing the maximum separation possible with the data at hand. We additionally
consider 2030–2049 vs. 1980–1999 variance ratios from the control run (Fig. 5, left column), which was integrated for 150
310 years with fixed forcing (Haarsma et al., 2016). These estimates give an approximate idea of the magnitude of regional p_b
changes that emerge internally within the simulations in the absence of time-evolving climate conditions. Evidently, the control
run variance ratios from the three models have very little in common and are mostly restricted to the range $R = 0.7$ – 1.3 , with
only a few broader statistically significant changes (e.g., in the Bellingshausen Basin for HadGEM). These findings provide
useful context for to the discussion of climate-driven changes in the simulated p_b variance (see below). A region that needs to
315 be interpreted with caution, though, is the deep Arctic Ocean, which sees strengthened p_b variability in the control run of all
three models. However, that increase is statistically significant only in CNRM.

The maps of R formed using the CMIP6-HR historical and scenario runs (Fig. 5, right column) paint a relatively complex
picture of future changes in p_b variance. Amplitude decreases typically alternate with increases on sub-basin scales, involving
changes in regions with distinct dynamical regimes. Although the three maps show many differences in detail, we can still
320 discern a few common, statistically significant features that point to a robust response of dynamic p_b to climate change. One
such region appears to be the connected deep basin of the Arctic Ocean and Nordic Seas, with widespread variance increases
of 40–60%, partly also extending to adjacent continental shelves. The increase in CNRM, though, is smaller than in the control

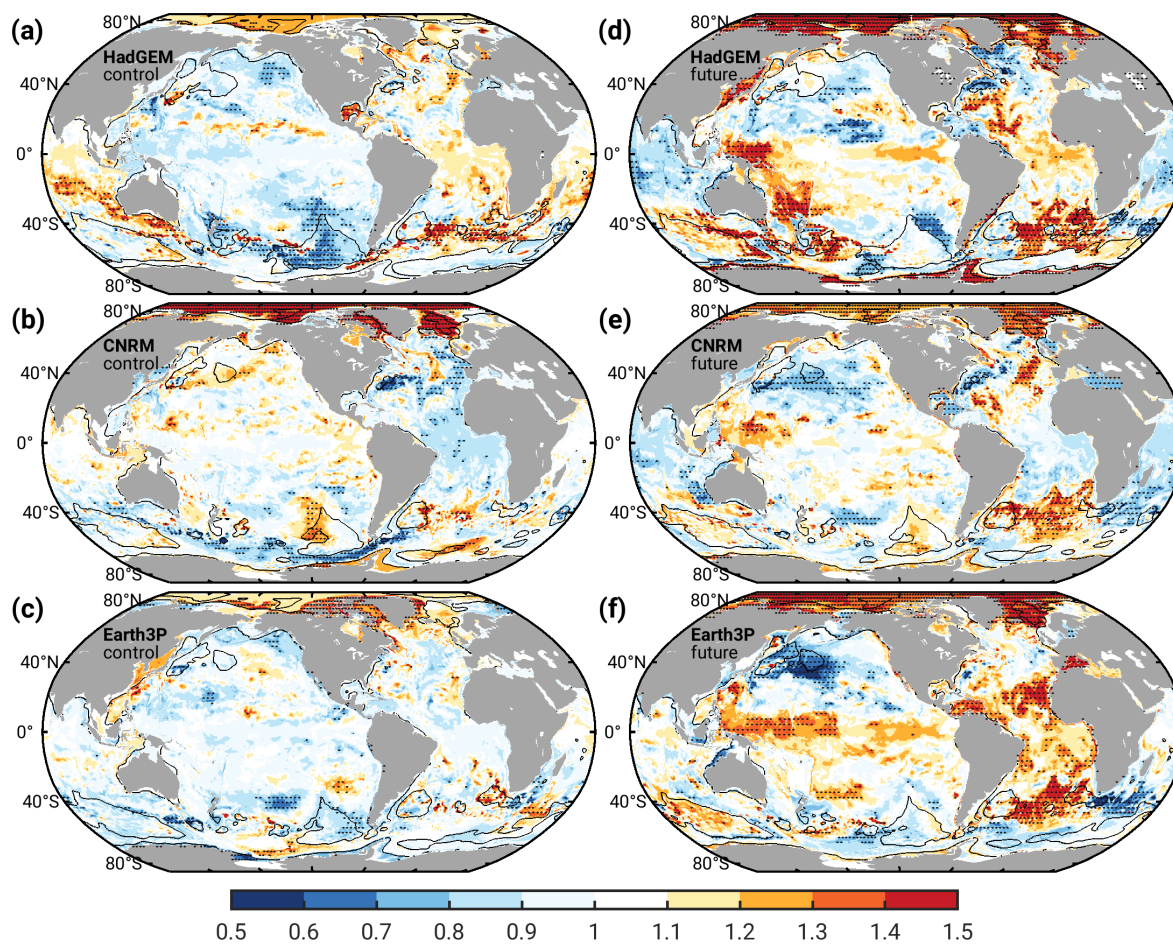


Figure 5. Dimensionless variance ratios of unfiltered p_b time series over the 2030–2049 time period relative 1980–1999 for HadGEM (top row), CNRM (middle row), and Earth3P (bottom row). Left panels (a–c) present the variance ratios for p_b from each model’s control simulation, whereas the right panels (d–f) show the ratios formed from the combined scenario and historical simulations. Stipples indicate $3^\circ \times 3^\circ$ cells where the variance ratio is significantly different from zero at 90% confidence for at least a third of the contained $1/4^\circ$ grid points (confidence levels were determined from the proper F -test considering the effective degrees of freedom at each grid point). Black contours encase areas where the model RMS in Fig. 2, smoothed to 200 km length scales, exceeds 3 cm.

run (Figs. 5b and 5e) and therefore questions the results from HadGEM and Earth3P. To examine the matter further—and given the tight connection of p_b fluctuations in the Arctic region to wind forcing (Fukumori et al., 2015)—we plot projected changes in the zonally averaged 10-m wind speed from the three CMIP6-HR simulations (Fig. 6, 2030–2049 relative to 1980–1999 as before). All three models suggest enhanced surface wind speeds poleward of 60°N by 2030–2049, but in CNRM the climate-induced signal is indiscriminate from internal variability (as quantified by means of the control run; blacked dashed line in Fig. 6b). However, similar analyses of high-latitude surface wind speeds from most available 1° CMIP6 models (Liu et al.,

325

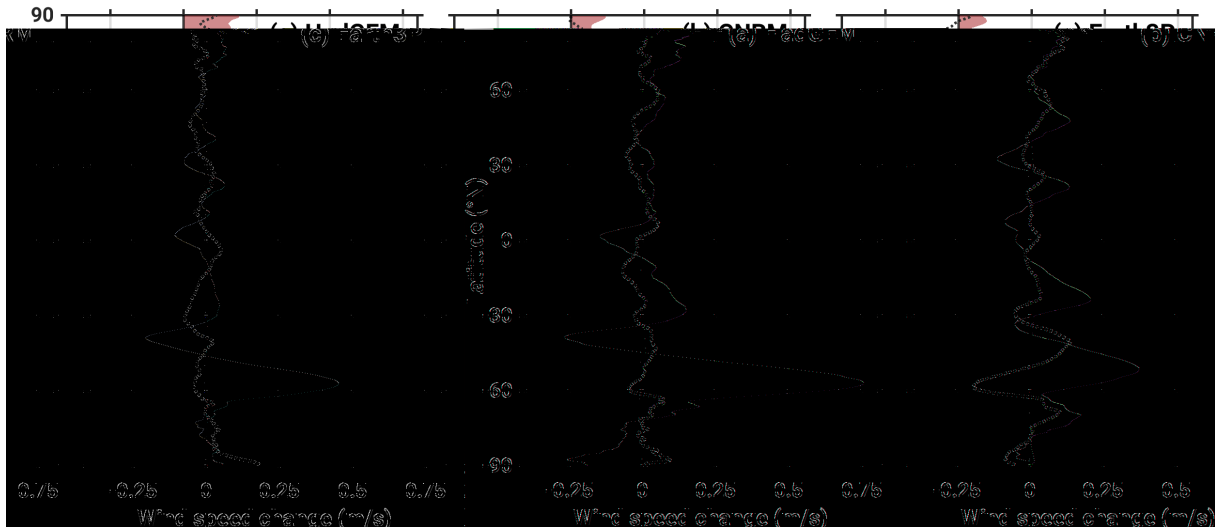


Figure 6. Change in zonally averaged global surface wind speed by 2030–2049 relative to 1980–1999 from the (a) HadGEM, (b) CNRM, and (c) Earth3P simulations (unit is m s^{-1} , land areas are included). Colored meridional profiles show the results from the scenario and historical runs (cf. Fig. 5), while the black dotted line indicates the corresponding profile from the control run.

2024; Zhang and Wang, 2024) rather favor the strengthening evident in HadGEM and Earth3P. We therefore conclude that the
330 increase in simulated Arctic p_b variability by the mid of the 21st century is indeed attributable to anthropogenic forcing and
specifically caused by accelerated surface winds.

Along with some interesting cases of diminishing amplitudes (e.g., Northwest Pacific, Gulf Stream region), we find an
intensification of p_b variability under SSP5-8.5 in the western tropical Pacific. North of New Guinea, values of R peak at
 $R \approx 1.3$ – 1.5 . The area is characterized by low-magnitude p_b signals (Figs. 1 and 2), induced by a mix of both barotropic and
335 baroclinic processes that tend to be most active at annual and semiannual frequencies (e.g., Qu et al., 2008; Piecuch et al.,
2015; Cheng et al., 2021). Indeed, the patch of intensified p_b amplitudes in the western tropical Pacific vanishes when variance
ratios are formed based on non-seasonal model time series (Supplementary Fig. S1). Although more definitive diagnosis of the
processes at work is beyond our scope, we note that large parts of the tropical Pacific Ocean have positive values of R in both
HadGEM and Earth3P. This in turn hints at changes in local Ekman pumping or wind-driven Rossby waves, possibly related
340 to increases in stratification or migration of the Inter-Tropical Convergence Zone (cf. Qu et al., 2008; Piecuch et al., 2015).

The third salient feature in Fig. 5, seen across all three models, is a mid-21st century intensification of ~ 30 – 60% in p_b
variance in the South Atlantic. The patch of red color sits between the Zapiola Gyre and Cape Basin (cf. Fig. 1) and is
accompanied in eastward direction by a decrease in p_b variability over the Agulhas Return Current. These structures are
consistent with the patterns of projected changes in the regions's eddy kinetic energy, as implied by future climate simulations
345 (Beech et al., 2022; Wang et al., 2024). In particular, global warming is expected to strengthen Southern Hemisphere westerlies
and progressively shift them to the south (Deng et al., 2022, see also Fig. 6), thus weakening westerly winds around the



southern coast of Africa ($\sim 35^\circ\text{S}$). Decelerated winds will in turn reduce volume transport and eddy kinetic energy in the Agulhas Current, while also leading to increases in Agulhas leakage and mesoscale activity in the South Atlantic (Biaostoch et al., 2009; van Sebille et al., 2009; Beech et al., 2022). That these dynamics imprint on p_b is clear from Fig. 2 and previous
350 model analyses (Hughes et al., 2018; Zhao et al., 2021). In addition, climate change invigorates eddy activity in the western part of the basin (Beech et al., 2022), and that too could contribute to the enhanced future p_b variance seen in Fig. 5. Thus, the South Atlantic and Agulhas Return Current region appear to be an interesting laboratory for linking long-term changes in p_b variability with anthropogenic impacts on the ocean circulation.

4 Summary and conclusions

355 We have run basic and mostly global assessments of bottom pressure signals in CMIP6-HR simulations, motivated in large part by the potential use of these fields in satellite gravimetry simulation studies. The climate models capture all relevant p_b phenomena that can be expected to emerge at the given resolution and under the encoded physics, e.g., eddy structures and wind-driven variability on continental shelves and in the deep ocean. Model accuracy, as evaluated through comparisons to a downscaled GRACE product and BPR measurements, varies with latitude, depth, frequency, and more generally the specific
360 dynamical regime (Figs 2 and 3, Table 2). In particular, the CMIP6-HR models tested here are susceptible to overestimation of topographically constrained p_b variability, most notably in the Australian-Antarctic and Weddell-Enderby Abyssal plains and at seasonal frequencies. Similar issues are apparent in NEMO-based ocean reanalyses on the ORCA025 grid (cf. Figure 3 in Gou et al., 2025), pointing to structural errors in that particular ocean model setup. As suggested in Sect. 3.2, the excess variance may have diverse causes, including imperfect momentum transfer schemes, coarse vertical spacing of deep layers, and
365 the artificial blocking of ice shelf cavities. In this light, analysis of p_b variability may be useful to guide model improvements or at least complement the standard tests of near-surface variables and meridional overturning (e.g., Zuo et al., 2017; Roberts et al., 2019, 2020).

We have exercised a degree of caution in our comparisons of the CMIP6-HR p_b fields against GRACE-DS and BPRs. Neither reference dataset is free of error, whereas the models only approximate reality and thus disregard several legitimate contribu-
370 tions to the observed p_b changes (e.g., GAL, barometric pressure-driven dynamics, sub-grid scale variability). These issues can compromise the model-data comparison, particularly in very quiet deep-ocean regions (Fig. 3) and at individual BPRs (Fig. 4). The spatial median statistics in Table 2 are nonetheless conclusive and internally consistent enough to discriminate more accurate models from less realistic p_b representations. Specifically, in satellite gravimetry simulations, where one would want to portray oceanic mass changes across all spatial and temporal scales, the HighResMIP contribution of Earth3P appears
375 to be a very sensible choice. One caveat is that compared to the models (analyzed over 1980–2014), the BPR and GRACE-DS variance estimates are taken over different and much shorter time periods, i.e., 2013–2023 and ~ 2002 –2020. However, when narrowing the model time series to 2002–2014 (Supplementary Table S1), our basic conclusions drawn from Table 2 remained unchanged, except for low-latitude shelf regions. The agreement is not unexpected, because the climatic conditions over the



CMIP6-HR late historical period do not evolve as drastically as they do in the scenario extension to 2049, implying temporal
380 changes in p_b variance that are well below those shown in Fig. 5d–f.

Our model-based diagnosis of future climate impacts on the strength of p_b fluctuations has added a new facet to the existing
bottom pressure literature. While these impacts are spread over regions characterized by very different dynamics (i.e., Arctic,
tropical Pacific, Agulhas leakage), an origin in altered wind forcing (Fig. 6) is likely common to all three cases. Dedicated
modeling work, such as stand-alone ocean simulations under distinct forcing assumptions, will be required to shed light on
385 the exact processes at work. More generally, the reported strengthening of regional p_b variability awaits confirmation through
analysis of output from other climate models and perhaps, at some point, also through actual observations. Here we have
made our inferences based on variance metrics in bi-decadal windows 50 years apart, but the noted p_b amplitude increases in
the Arctic, tropical Pacific, and parts South Atlantic also emerge when using a reference periods shifted forward by 15 years
(1995–2014, Supplementary Fig. S2). Thus, given the planned continuity of space-based mass change monitoring (Daras et al.,
390 2024), climate-driven changes in large-scale, dynamic p_b variability may be soon detectable with satellite gravimetry.

Data availability. The datasets used in this study are available from the following links: CMIP6 HighResMIP output (<https://esgf-data.dkrz.de/search/cmip6-dkrz/>), GRACE-DS (<https://doi.org/10.3929/ethz-b-000686843> Gou et al., 2024), DART[®] historical data (https://www.ndbc.noaa.gov/historical_data.shtml), and ECCOv4r4b (<https://cmr.earthdata.nasa.gov/virtual-directory/collections/C2129193421-POCLOUD>). Monthly p_b fields from all five CMIP6-HR models analyzed in this study have been placed at <https://doi.org/10.5281/zenodo.14886818> (Liu
395 et al., 2025).

Author contributions. **L. L.:** Data curation, Formal analysis, Investigation, Methodology, Software, Visualization, Writing - original draft, Writing - review & editing. **M. S.:** Conceptualization, Funding acquisition, Methodology, Supervision, Validation, Writing - original draft, Writing - review & editing. **L. B.:** Software, Writing - review & editing. **J. F.:** Formal analysis, Software, Writing - review & editing. **J. G.:** Methodology, Writing - review & editing.

400 *Competing interests.* The authors declare no conflict of interests.

Acknowledgements. This study was supported by the German Research Foundation (DFG, Project nos. 388296632 and 459392861), and represents a contribution to the New Refined Observations of Climate Change from Spaceborne Gravity Missions (NEROGRAM) project.



References

- Adcroft, A., Hughes, C., and Marshall, J.: Representation of topography by shaved cells in height coordinate ocean model, *Mon. Weather Rev.*, 125, 2293–2315, [https://doi.org/10.1175/1520-0493\(1997\)125<2293:ROTBSC>2.0.CO;2](https://doi.org/10.1175/1520-0493(1997)125<2293:ROTBSC>2.0.CO;2), 1997.
- Amante, C. and Eakins, B. W.: ETOPO1 1 Arc-Minute Global Relief Model: Procedures, Data Sources and Analysis. NOAA Technical Memorandum NESDIS NGDC-24, <https://doi.org/10.7289/V5C8276M>, 2009.
- Androsov, A., Boebel, O., Schröter, J., Danilov, S., Macrander, A., and Ivanciu, I.: Ocean bottom pressure variability: Can it be reliably modeled?, *J. Geophys. Res. Oceans*, 125, e2019JC015469, <https://doi.org/10.1029/2019JC015469>, 2020.
- 405 Beech, N., Rackow, T., Semmler, T., Danilov, S., Wang, Q., and Jung, T.: Long-term evolution of ocean eddy activity in a warming world, *Nat. Clim. Change*, 12, 910–917, <https://doi.org/10.1038/s41558-022-01478-3>, 2022.
- Bernard, B., Madec, G., Penduff, T., Molines, J.-M., Treguier, A.-M., Le Sommer, J., Beckmann, A., Biastoch, A., Böning, C., Dengg, J., Derval, C., Durand, E., Gulev, S., Remy, E., Talandier, C., Theeten, M., McClean, J., and De Cuevas, B.: Impact of partial steps and momentum advection schemes in a global ocean circulation model at eddy-permitting resolution, *Ocean Dynam.*, 56, 543–567, <https://doi.org/doi.org/10.1007/s10236-006-0082-1>, 2006.
- 415 Bernard, E. N. and Meinig, C.: History and future of deep-ocean tsunami measurements, in: *Proceedings of Oceans'11 MTS/IEEE Kona*, 6106894, pp. 1–7, IEEE, 2011.
- Biastoch, A., Böning, C. W., Schwarzkopf, F. U., and Lutjeharms, J. R. E.: Increase in Agulhas leakage due to poleward shift of Southern Hemisphere westerlies, *Nature*, 462, 495–498, <https://doi.org/10.1038/nature08519>, 2009.
- 420 Bingham, R. and Hughes, C.: The relationship between sea-level and bottom pressure variability in an eddy-permitting ocean model, *Geophys. Res. Lett.*, 35, L03602, <https://doi.org/10.1029/2007GL032662>, 2008.
- Bingham, R. J. and Haines, K.: Decadal ocean bottom pressure variability and its associated gravitational effects in a coupled ocean-atmosphere model, in: *Gravity, Geoid and Space Missions: GGSM 2004 IAG International Symposium Porto*, pp. 298–303, Springer, https://doi.org/10.1007/3-540-26932-0_52, 2005.
- 425 Boening, C., Lee, T., and Zlotnicki, V.: A record-high ocean bottom pressure in the South Pacific observed by GRACE, *Geophys. Res. Lett.*, 38, L04602, <https://doi.org/10.1029/2010GL046013>, 2011.
- Börger, L., Schindelegger, M., Dobsław, H., and Salstein, D.: Are ocean reanalyses useful for Earth rotation research?, *Earth Space Sci.*, 10, e2022EA002700, <https://doi.org/10.1029/2022EA002700>, 2023.
- Chen, L., Yang, J. Y., and Wu, L. X.: Topography effects on the seasonal variability of ocean bottom pressure in the North Pacific Ocean, *J. Phys. Oceanogr.*, 53, 929–941, <https://doi.org/10.1175/JPO-D-22-0140.1>, 2023.
- 430 Cheng, X., Ou, N. S., Chen, J. J., and Huang, R. X.: On the seasonal variations of ocean bottom pressure in the world oceans, *Geosci. Lett.*, 8, 29, <https://doi.org/10.1186/s40562-021-00199-3>, 2021.
- Cherchi, A., Fogli, P. G., Lovato, T., Peano, D., Iovino, D., Gualdi, S., Masina, S., Scoccimarro, E., Materia, S., Bellucci, A., and Navarra, A.: Global mean climate and main patterns of variability in the CMCC-CM2 coupled model, *J. Adv. Model. Earth Sy.*, 11, 185–209, <https://doi.org/10.1029/2018MS001369>, 2019.
- 435 Daras, I., March, G., Pail, R., Hughes, C. W., Braitenberg, C., Güntner, A., Eicker, A., Wouters, B., Heller-Kaikov, B., Pivetta, T., and Pastorutti, A.: Mass-change And Geosciences International Constellation (MAGIC) expected impact on science and applications, *Geophys. J. Int.*, 236, 1288–1308, <https://doi.org/10.1093/gji/ggad472>, 2024.



- De Linage, C., Rivera, L., Hinderer, J., Boy, J.-P., Rogister, Y., Lambotte, S., and Biancale, R.: Separation of coseismic and postseismic
440 gravity changes for the 2004 Sumatra–Andaman earthquake from 4.6 yr of GRACE observations and modelling of the coseismic change
by normal-modes summation, *Geophys. J. Int.*, 176, 695–714, <https://doi.org/10.1111/j.1365-246X.2008.04025.x>, 2009.
- de Miranda, A. P., Barnier, B., and Dewar, W. K.: On the dynamics of the Zapiola Anticyclone, *J. Geophys. Res. Oceans*, 104, 21 137–21 149,
<https://doi.org/10.1029/1999JC900042>, 1999.
- Deng, K., Azorin-Molina, C., Yang, S., Hu, C., Zhang, G., Minola, L., and Chen, D.: Changes of Southern Hemisphere westerlies in the
445 future warming climate, *Atmos. Res.*, 270, 106 040, <https://doi.org/10.1016/j.atmosres.2022.106040>, 2022.
- Docquier, D., Grist, J. P., Roberts, M. J., Roberts, C. D., Semmler, T., Ponsoni, L., Massonnet, F., Sidorenko, D., Sein, D. V., Iovino, D.,
Bellucci, A., and Fichefet, T.: Impact of model resolution on Arctic sea ice and North Atlantic Ocean heat transport, *Clim. Dynam.*, 53,
4989–5017, <https://doi.org/10.1007/s00382-019-04840-y>, 2019.
- Forget, G., Campin, J. M., Heimbach, P., Hill, C. N., Ponte, R. M., and Wunsch, C.: ECCO version 4: an integrated framework for non-linear
450 inverse modeling and global ocean state estimation, *Geosci. Model Dev.*, 8, <https://doi.org/10.5194/gmd-8-3071-2015>, 2015.
- Fukumori, I., Raghunath, R., and Fu, L. L.: Nature of global large-scale sea level variability in relation to atmospheric forcing: A modeling
study, *J. Geophys. Res. Oceans*, 103, 5493–5512, <https://doi.org/10.1029/97JC02907>, 1998.
- Fukumori, I., Wang, O., Llovel, W., Fenty, I., and Forget, G.: A near-uniform fluctuation of ocean bottom pressure and
sea level across the deep ocean basins of the Arctic Ocean and the Nordic Seas, *Prog. Oceanogr.*, 134, 152–172,
455 <https://doi.org/10.1016/j.pocean.2015.01.0135>, 2015.
- Gill, A. E. and Niller, P. P.: The theory of the seasonal variability in the ocean, *Deep Sea Res. Oceanogr. Abstr.*, 20, 141–177,
[https://doi.org/10.1016/0011-7471\(73\)90049-1](https://doi.org/10.1016/0011-7471(73)90049-1), 1973.
- Gou, J. Y., Börger, L., Schindelegger, M., and Soja, B.: SeDA-OBP: Global ocean bottom pressure anomaly fields with a spatial resolution
of 0.25 degrees from self-supervised data assimilation, *ETH Research Collection*, <https://doi.org/10.3929/ethz-b-000686843>, 2024.
- 460 Gou, J. Y., Börger, L., Schindelegger, M., and Soja, B.: Downscaling GRACE-derived ocean bottom pressure anomalies using self-supervised
data fusion, *J. Geodesy*, 99, 19, <https://doi.org/10.1007/s00190-025-01943-9>, 2025.
- Haarsma, R., Acosta, M., Bakhshi, R., Bretonnière, P.-A., Caron, L.-P., Castrillo, M., Corti, S., Davini, P., Exarchou, E., Fabiano, F., Fladrich,
U., Fuentes Franco, R., García-Serrano, J., von Hardenberg, J., Koenigk, T., Levine, X., Meccia, V. L., van Noije, T., van den Oord, G.,
Palmeiro, F. M., Rodrigo, M., Ruprich-Robert, Y., Le Sager, P., Tourigny, E., Wang, S., van Weele, M., and Wyser, K.: HighResMIP
465 versions of EC-Earth: EC-Earth3P and EC-Earth3P-HR – description, model computational performance and basic validation, *Geosci.
Model Dev.*, 13, 3507–3527, <https://doi.org/10.5194/gmd-13-3507-2020>, 2020.
- Haarsma, R. J., Roberts, M. J., Vidale, P. L., Senior, C. A., Bellucci, A., Bao, Q., Chang, P., Corti, S., Fučkar, N. S., Guemas, V., von Harden-
berg, J., Hazeleger, W., Kodama, C., Koenigk, T., Leung, L. R., Lu, J., Luo, J.-J., Mao, J., Mizielinski, M. S., Mizuta, R., Nobre, P., Satoh,
M., Scoccimarro, E., Semmler, T., Small, J., and von Storch, J.-S.: High Resolution Model Intercomparison Project (HighResMIP v1.0)
470 for CMIP6, *Geosci. Model Dev.*, 9, 4185–4208, <https://doi.org/10.5194/gmd-9-4185-2016>, 2016.
- Harker, A. A., Schindelegger, M., Ponte, R. M., and Salstein, D. A.: Modeling ocean-induced rapid Earth rotation variations: An update, *J.
Geodesy*, 95, 110, <https://doi.org/10.1007/s00190-021-01555-z>, 2021.
- Hart-Davis, M. G., Piccioni, G., Dettmering, D., Schwatke, C., Passaro, M., and Seitz, F.: EOT20: A global ocean tide model from multi-
mission satellite altimetry, *Earth Syst. Sci. Data*, 13, 3869–3884, <https://doi.org/10.5194/essd-13-3869-2021>, 2021.
- 475 Hersbach, H., Bell, B., Berrisford, P., Hirahara, S., Horányi, A., Muñoz-Sabater, J., Nicolas, J., Peubey, C., Radu, R., Schepers, D., Simmons,
A., Soci, C., Abdalla, S., Abellan, X., Balsamo, G., Bechtold, P., Biavati, G., Bidlot, J., Bonavita, M., De Chiara, G., Dahlgren, P., Dee,



- D., Diamantakis, M., Dragani, R., Flemming, J., Forbes, R., Fuentes, M., Geer, A., Haimberger, L., Healy, S., Hogan, R. J., Hólm, E., Janisková, M., Keeley, S., Laloyaux, P., Lopez, P., Lupu, C., Radnoti, G., de Rosnay, P., Rozum, I., Vamborg, F., Villaume, S., and Thépaut, J.-N.: The ERA5 global reanalysis, *Q. J. Roy. Astron. Soc.*, 146, 1999–2049, <https://doi.org/10.1002/qj.3803>, 2020.
- 480 Hughes, C. W., Stepanov, V. N., Fu, L. L., Barnier, B., and Hargreaves, G. W.: Three forms of variability in Argentine Basin ocean bottom pressure, *J. Geophys. Res. Oceans*, 112, <https://doi.org/10.1029/2006JC003679>, 2007.
- Hughes, C. W., Williams, J., Blaker, A., Coward, A., and Stepanov, V.: A window on the deep ocean: The special value of ocean bottom pressure for monitoring the large-scale, deep-ocean circulation, *Prog. Oceanogr.*, 161, 19–46, <https://doi.org/10.1016/j.pocean.2018.01.011>, 2018.
- 485 Hughes, C. W., Fukumori, I., Griffies, S. M., Huthnance, J. M., Minobe, S., Spence, P., Thompson, K. R., and Wise, A.: Sea level and the role of coastal trapped waves in mediating the influence of the open ocean on the coast, *Surv. Geophys.*, 40, 1467–1492, <https://doi.org/10.1007/s10712-019-09535-x>, 2019.
- Jensen, L., Eicker, A., Dobslaw, H., and Pail, R.: Emerging changes in terrestrial water storage variability as a target for future satellite gravity missions, *Remote Sens.*, 12, 3898, <https://doi.org/10.3390/rs12233898>, 2020.
- 490 Johnson, G. C. and Chambers, D. P.: Ocean bottom pressure seasonal cycles and decadal trends from GRACE Release-05: Ocean circulation implications, *J. Geophys. Res. Oceans*, 118, 4228–4240, <https://doi.org/10.1002/jgrc.20307>, 2013.
- Kemp, J., Newhall, K., Ostrom, W., Krishfield, R., and Proshutinsky, A.: The Beaufort Gyre observing system 2004: Mooring recovery and deployment operations in pack ice, Woods Hole Oceanographic Institution, 2005.
- Kvas, A., Behzadpour, S., Ellmer, M., Klinger, B., Strasser, S., Zehentner, N., and Mayer-Gürr, T.: ITSG-Grace2018: Overview and evaluation of a new GRACE-only gravity field time series, *J. Geophys. Res. Sol. Ea.*, 124, 9332–9344, <https://doi.org/10.1029/2019JB017415>, 2019.
- 495 Landerer, F. W., Jungclaus, J. H., and Marotzke, J.: Ocean bottom pressure changes lead to a decreasing length-of-day in a warming climate, *Geophys. Res. Lett.*, 34, L06307, <https://doi.org/10.1029/2006GL029106>, 2007.
- Lellouche, J.-M., Le Galloudec, O., Drévilion, M., Régnier, C., Greiner, E., Garric, G., Ferry, N., Desportes, C., Testut, C.-E., Bricaud, C., Bourdallé-Badie, R., Tranchant, B., Benkiran, M., Drillet, Y., Daudin, A., and De Nicola, C.: Evaluation of global monitoring and forecasting systems at Mercator Océan, *Ocean Sci.*, 9, 57–81, <https://doi.org/10.5194/os-9-57-2013>, 2013.
- 500 Liu, L., Schindelegger, M., and Börger, L.: Monthly ocean bottom pressure anomalies 1980–2014 and 2030–2049 from CMIP6 HighResMIP models, *Zenodo*, <https://doi.org/10.5281/zenodo.14886818>, 2025.
- Liu, W., Yang, S., Chen, D., Zha, J., Zhang, G., Zhang, Z., Zhang, T., Xu, L., Hu, X., and Deng, K.: Rapid acceleration of Arctic near-surface wind speed in a warming climate, *Geophys. Res. Lett.*, 51, e2024GL109385, <https://doi.org/10.1029/2024GL109385>, 2024.
- 505 Ludwigsen, C. B., Andersen, O. B., Marzeion, B., Malles, J.-H., Müller Schmied, H., Döll, P., Watson, C., and King, M. A.: Global and regional ocean mass budget closure since 2003, *Nat. Commun.*, 15, 1416, <https://doi.org/10.1038/s41467-024-45726-w>, 2024.
- Madec, G.: NEMO reference manual 3.6_STABLE: NEMO ocean engine, Institut Pierre-Simon Laplace (IPSL), France, 2016.
- Makowski, J. K., Chambers, D. P., and Bonin, J. A.: Using ocean bottom pressure from the gravity recovery and climate experiment (GRACE) to estimate transport variability in the southern Indian Ocean, *J. Geophys. Res. Oceans*, 120, 4245–4259, <https://doi.org/10.1002/2014JC010575>, 2015.
- 510 McDougall, T. J. and Barker, P. M.: Getting started with TEOS-10 and the Gibbs Seawater (GSW) oceanographic toolbox, *Scor/Iapso WG*, 127, 1–28, 2011.
- Oliver, E. C. J. and Thompson, K. R.: Sea level and circulation variability of the Gulf of Carpentaria: Influence of the Madden-Julian Oscillation and the adjacent deep ocean, *J. Geophys. Res. Oceans*, 116, C02019, <https://doi.org/10.1029/2010JC006596>, 2011.



- 515 O'Neill, B. C., Tebaldi, C., van Vuuren, D. P., Eyring, V., Friedlingstein, P., Hurtt, G., Knutti, R., Kriegler, E., Lamarque, J.-F., Lowe, J., Meehl, G. A., Moss, R., Riahi, K., and Sanderson, B. M.: The Scenario Model Intercomparison Project (ScenarioMIP) for CMIP6, *Geosci. Model Dev.*, 9, 3461–3482, <https://doi.org/10.5194/gmd-9-3461-2016>, 2016.
- Petrick, C., Dobslaw, H., Bergmann-Wolf, I., Schön, N., Matthes, K., and Thomas, M.: Low-frequency ocean bottom pressure variations in the North Pacific in response to time-variable surface winds, *J. Geophys. Res. Oceans*, 119, 5190–5202, <https://doi.org/10.1002/2013JC009635>, 2014.
- 520 Piecuch, C. G.: Bottom-pressure signature of annual baroclinic Rossby waves in the northeast tropical Pacific Ocean, *J. Geophys. Res. Oceans*, 120, 2449–2459, <https://doi.org/10.1002/2014JC010667>, 2015.
- Piecuch, C. G., Fukumori, I., Ponte, R. M., and Wang, O.: Vertical structure of ocean pressure variations with application to satellite-gravimetric observations, *J. Atmos. Ocean. Tech.*, 32, 603–613, <https://doi.org/10.1175/JTECH-D-14-00156.1>, 2015.
- 525 Piecuch, C. G., Fukumori, I., Ponte, R. M., Schindelegger, M., Wang, O., and Zhao, M.: Low-frequency dynamic ocean response to barometric-pressure loading, *J. Phys. Oceanogr.*, 52, 2627–2641, <https://doi.org/10.1175/JPO-D-22-0090.1>, 2022.
- Ponte, R. M.: Variability in a homogeneous global ocean forced by barometric pressure, *Dynam. Atmos. Ocean.*, 18, 209–234, [https://doi.org/10.1016/0377-0265\(93\)90010-5](https://doi.org/10.1016/0377-0265(93)90010-5), 1993.
- Ponte, R. M.: A preliminary model study of the large-scale seasonal cycle in bottom pressure over the global ocean, *J. Geophys. Res. Oceans*, 104, 1289–1300, <https://doi.org/10.1029/1998JC900028>, 1999.
- 530 Ponte, R. M. and Piecuch, C. G.: Interannual bottom pressure signals in the Australian–Antarctic and Bellingshausen basins, *J. Phys. Oceanogr.*, 44, 1456–1465, <https://doi.org/10.1175/JPO-D-13-0223.1>, 2014.
- Ponte, R. M., Rajamony, J., and Gregory, J. M.: Ocean angular momentum signals in a climate model and implications for Earth rotation, *Clim. Dynam.*, 19, 181–190, <https://doi.org/10.1007/s00382-001-0216-6>, 2002.
- 535 Ponte, R. M., Zhao, M., and Schindelegger, M.: How well do we know the seasonal cycle in ocean bottom pressure?, *Earth Space Sci.*, 11, e2024EA003661, <https://doi.org/10.1029/2024EA003661>, 2024.
- Poropat, L., Dobslaw, H., Zhang, L., Macrander, A., Boebel, O., and Thomas, M.: Time variations in ocean bottom pressure from a few hours to many years: In situ data, numerical models, and GRACE satellite gravimetry, *J. Geophys. Res. Oceans*, 123, 5612–5623, <https://doi.org/10.1029/2018JC014108>, 2018.
- 540 Qu, T., Gan, J., Ishida, A., Kashino, Y., and Tozuka, T.: Semiannual variation in the western tropical Pacific Ocean, *Geophys. Res. Lett.*, 35, L16602, <https://doi.org/10.1029/2008GL035058>, 2008.
- Ray, R. D., Loomis, B. D., and Zlotnicki, V.: The mean seasonal cycle in relative sea level from satellite altimetry and gravimetry, *J. Geodesy*, 95, 80, <https://doi.org/10.1007/s00190-021-01529-1>, 2021.
- Roberts, C., Senan, R., Molteni, F., Boussetta, S., Mayer, M., and Keeley, S.: Climate model configurations of the ECMWF Integrated Forecasting System (ECMWF-IFS cycle 43r1) for HighResMIP, *Geosci. Model Dev.*, 11, 3681–3712, <https://doi.org/10.5194/gmd-11-3681-2018>, 2018.
- 545 Roberts, M. J., Baker, A., Blockley, E. W., Calvert, D., Coward, A., Hewitt, H. T., Jackson, L. C., Kuhlbrodt, T., Mathiot, P., Roberts, C. D., Schiemann, R., Seddon, J., Vanni ere, B., and Vidale, P. L.: Description of the resolution hierarchy of the global coupled HadGEM3-GC3.1 model as used in CMIP6 HighResMIP experiments, *Geosci. Model Dev.*, 12, 4999–5028, <https://doi.org/10.5194/gmd-12-4999-2019>, 2019.
- 550 Roberts, M. J., Jackson, L. C., Roberts, C. D., Meccia, V., Docquier, D., Koenigk, T., Ortega, P., Moreno-Chamarro, E., Bellucci, A., Coward, A., Drijfhout, S., Exarchou, E., Gutjahr, O., Hewitt, H., Iovino, D., Lohmann, K., Putrasahan, D., Schiemann, R., Seddon, J., Terray, L.,



- Xu, X., Zhang, Q., Chang, P., Yeager, S. G., Castruccio, F. S., Zhang, S., and Wu, L.: Sensitivity of the Atlantic Meridional Overturning Circulation to model resolution in CMIP6 HighResMIP simulations and implications for future changes, *J. Adv. Model. Earth Sy.*, 12, e2019MS002014, <https://doi.org/10.1029/2019MS002014>, 2020.
- 555 Save, H., Bettadpur, S., and Tapley, B. D.: High-resolution CSR GRACE RL05 mascons, *J. Geophys. Res. Sol. Ea.*, 121, 7547–7569, <https://doi.org/10.1002/2016JB013007>, 2016.
- Schindelegger, M., Harker, A. A., Ponte, R. M., Dobsław, H., and Salstein, D. A.: Convergence of daily GRACE solutions and models of submonthly ocean bottom pressure variability, *J. Geophys. Res. Oceans*, 126, e2020JC017031, <https://doi.org/10.1029/2020JC017031>,
560 2021.
- Sen Gupta, A., Jourdain, N. C., Brown, J. N., and Monselesan, D.: Climate drift in the CMIP5 models, *J. Climate*, 26, 8597–8615, <https://doi.org/10.1175/JCLI-D-12-00521.1>, 2013.
- Shi, J. R., Talley, L. D., Xie, S. P., Peng, Q. H., and Liu, W.: Ocean warming and accelerating Southern Ocean zonal flow, *Nat. Clim. Change*, 11, 1090–1097, <https://doi.org/10.1038/s41558-021-01212-5>, 2021.
- 565 Shihora, L., Balidakis, K., Dill, R., Dahle, C., Ghobadi-Far, K., Bonin, J., and Dobsław, H.: Non-tidal background modeling for satellite gravimetry based on operational ECWMF and ERA5 reanalysis data: AOD1B RL07, *J. Geophys. Res. Sol. Ea.*, 127, e2022JB024360, <https://doi.org/10.1029/2022JB024360>, 2022.
- Storkey, D., Blaker, A. T., Mathiot, P., Megann, A., Aksenov, Y., Blockley, E. W., Calvert, D., Graham, T., Hewitt, H. T., Hyder, P., Kuhlbrodt, T., Rae, J. G. L., and Sinha, B.: UK Global Ocean GO6 and GO7: A traceable hierarchy of model resolutions, *Geosci. Model Dev.*, 11, 3187–3213, <https://doi.org/10.5194/gmd-11-3187-2018>, 2018.
- 570 Tapley, B. D., Watkins, M. M., Flechtner, F., Reigber, C., Bettadpur, S., Rodell, M., Sasgen, I., Famiglietti, J. S., Landerer, F. W., Chambers, D. P., Reager, J. T., Gardner, A. S., Himanshu, S., Ivins, E. R., Swenson, S. C., Boening, C., Dahle, C., Wiese, D. N., Dobsław, H., Tamisiea, M. E., and Velicogna, I.: Contributions of GRACE to understanding climate change, *Nat. Clim. Change*, 9, 358–369, <https://doi.org/10.1038/s41558-019-0456-2>, 2019.
- 575 van Dam, T., Collilieux, X., Wuite, J., Altamimi, Z., and Ray, J.: Nontidal ocean loading: amplitudes and potential effects in GPS height time series, *J. Geodesy*, 86, 1043–1057, <https://doi.org/10.1007/s00190-012-0564-5>, 2012.
- van Sebille, E., Biastoch, A., Van Leeuwen, P., and De Ruijter, W.: A weaker Agulhas Current leads to more Agulhas leakage, *Geophys. Res. Lett.*, 36, L03601, <https://doi.org/10.1029/2008GL036614>, 2009.
- Vinogradova, N. T., Ponte, R. M., and Stammer, D.: Relation between sea level and bottom pressure and the vertical dependence of oceanic variability, *Geophys. Res. Lett.*, 34, L03608, <https://doi.org/10.1029/2006GL028588>, 2007.
- 580 Voldoire, A., Saint-Martin, D., Sénési, S., Decharme, B., Alias, A., Chevallier, M., Colin, J., Guérémy, J.-F., Michou, M., Moine, M.-P., Nabat, P., Roehrig, R., Salas y Méliá, D., Séférian, R., Valcke, S., Beau, I., Belamari, S., Berthet, S., Cassou, C., Cattiaux, J., Deshayes, J., Douville, H., Ethé, C., Franchistéguy, L., Geoffroy, O., Lévy, C., Madec, G., Meurdesoif, Y., Msadek, R., Ribes, A., Sanchez-Gomez, E., Terray, L., and Waldman, R.: Evaluation of CMIP6 DECK experiments with CNRM-CM6-1, *J. Adv. Model. Earth Sy.*, 11, 2177–2213, <https://doi.org/10.1029/2019MS001683>, 2019.
- 585 Wang, S., Jing, Z., Wu, L., Sun, S., Chen, Z., Ma, X., and Gan, B.: A more quiescent deep ocean under global warming, *Nat. Clim. Change*, 14, 961–967, <https://doi.org/10.1038/s41558-024-02075-2>, 2024.
- Weijer, W.: Modal variability in the Southeast Pacific Basin: Energetics of the 2009 event, *Deep Sea Res. Pt. II*, 114, 3–11, <https://doi.org/10.1016/j.dsr2.2012.10.002>, 2015.



- 590 Weijer, W. and Gille, S. T.: Adjustment of the Southern Ocean to wind forcing on synoptic time scales, *J. Phys. Oceanogr.*, 35, 2076–2089,
<https://doi.org/10.1175/JPO2801.1>, 2005.
- Zhang, L., Tang, H., Chang, L., and Sun, W.: Performance of GRACE mascon solutions in studying seismic deformations, *J. Geophys. Res.*
Sol. Ea., 125, e2020JB019 510, <https://doi.org/10.1029/2020JB019510>, 2020.
- Zhang, Z. and Wang, K.: Quantify uncertainty in historical simulation and future projection of surface wind speed over global land and
595 ocean, *Environ. Res. Lett.*, 19, 054 029, <https://doi.org/10.1088/1748-9326/ad3e8f>, 2024.
- Zhao, M. N., Ponte, R. M., Penduff, T., Close, S., Llovel, W., and Molines, J. M.: Imprints of ocean chaotic intrinsic variability on bottom
pressure and implications for data and model analyses, *Geophys. Res. Lett.*, 48, e2021GL096 341, <https://doi.org/10.1029/2021GL096341>,
2021.
- Zhao, M. N., Ponte, R. M., and Penduff, T.: Global-scale random bottom pressure fluctuations from oceanic intrinsic variability, *Sci. Adv.*,
600 9, eadg0278, <https://doi.org/10.1126/sciadv.adg0278>, 2023.
- Zuo, H., Balmaseda, M. A., and Mogensen, K.: The new eddy-permitting ORAP5 ocean reanalysis: description, evaluation and uncertainties
in climate signals, *Clim. Dynam.*, 49, 791–811, <https://doi.org/10.1007/s00382-015-2675-1>, 2017.